

***Ab initio* tensile tests applied to bcc refractory alloys**Vishnu Raghuraman  and Michael Widom *Department of Physics, Carnegie Mellon University, Pittsburgh, Pennsylvania 15213, USA*Saro San *NETL Support Contractor, 1450 SW Queen Ave, Albany, Oregon 97321, USA*Michael C. Gao *National Energy Technology Laboratory, 1450 SW Queen Ave, Albany, Oregon 97321, USA*

(Received 6 September 2023; accepted 28 November 2023; published 11 December 2023)

Refractory metals exhibit high strength at high temperature, but often lack ductility. Multiprinciple element alloys such as high entropy alloys offer the potential to improve ductility while maintaining strength, but we do not know *a priori* what compositions will be suitable. A number of measures have been proposed to predict the ductility of metals, notably the Pugh ratio and the Rice-Thomson D-parameter, among others. Here we examine direct *ab initio* simulation of deformation under tensile strain, and we apply this to a variety of Nb- and Mo-based binary alloys and to several quaternary alloy systems. Our results exhibit peak stresses for elastic deformation, beyond which defects such as lattice slip, stacking faults, transformation, and twinning relieve the stress. The peak stress grows strongly with increasing valence electron count. Correlations are examined among several physical properties, including the above-mentioned ductility parameters.

DOI: [10.1103/PhysRevMaterials.7.123601](https://doi.org/10.1103/PhysRevMaterials.7.123601)**I. INTRODUCTION**

There is an ever-growing demand for alloys with high strength and ductility. Refractory high entropy alloys are potential candidates [1,2], with the added advantage of high melting points [3,4], but identifying suitable alloys among an extremely large sample space can be a challenge. First-principles approaches to alloy design offer a potentially simple and efficient way to screen for promising alloy compositions [5,6], which can then be synthesized and tested experimentally. While some mechanical properties such as bulk and shear modulus can be accurately determined by density functional theory (DFT) [7–9], ductility is much harder to predict [10] because distinct physical mechanisms enhance or diminish ductility, making it challenging to develop a single numerical parameter or test that is material agnostic. Additionally, extrinsic effects such as defects or impurities may mask the intrinsic ductility of a bulk single phase.

Experimentally, ductility can be estimated by performing a tensile test, where a sample of the alloy is subjected to uniaxial stress. Initially, the system deforms elastically—it returns to its undeformed shape on the removal of the applied uniaxial stress. When the applied stress exceeds the yield strength, the material deforms permanently. This is referred to as plastic deformation. On further application of stress, the system continues to deform plastically until it breaks. Ductility can be described as the ability of the system to undergo plastic deformation before tensile failure [11]. An alloy with a larger plastic region is considered to be more ductile.

The onset of plastic deformation can be triggered by several types of defects. A portion of the crystal may shear with respect to the other along a particular plane. This can

be caused by the passage of a dislocation that restores the crystalline order after lattice planes slip with respect to each other. The dislocation displacement and magnitude is represented by the Burgers vector. Plasticity may also be facilitated by stacking faults, which are errors in the arrangement of atomic planes and can be caused by the passage of partial dislocations [12,13]. Additionally, certain atoms may shear to produce a new equivalent crystal grain that shares a boundary with the original grain, but at a different orientation. This process, referred to as twinning [14], can contribute to the ductility of the system, as observed in twinning-induced plasticity (TWIP) steel [15]. Alternatively, the crystal may distort into an entirely new crystallographic structure, leading to transformation-induced plasticity (TRIP) [16,17]. Dislocation slip, deformation, and twinning compete and, depending on the system, any or all may facilitate plasticity.

A number of dimensionless measures have been proposed to predict the ductility of metals, notably the Pugh ratio of shear over bulk modulus [18], and the Rice-Thomson D-parameter given by the ratio of unstable stacking fault energy to surface energy [19–23]. Another dimensionless parameter  $\chi$  related to the strain thresholds for mechanical instabilities was recently proposed [24,25]. Each of these can be readily calculated *ab initio*, yet none proves fully satisfactory. Here we evaluate the utility of an *ab initio* tensile test in which we relax structures under increasing tensile strains and follow their mechanical stability and deformation. This approach can supplement the information obtained from the dimensionless parameters. In particular, it reveals peak stresses beyond which lattice slip, stacking faults, structural transformation, twinning, and other deformations relieve the stress, potentially aiding in ductility.

We apply this computational technique to study refractory Mo- and Nb-based bcc binary and quaternary alloys under tension along the [001] direction. Along with the peak stress, we calculate the valence electron count, the Pugh ratio, and the  $D$  and  $\chi$  parameters. In addition, we calculate the Fermi level electronic density of states, which reveals the balance of metallic vs covalent bonding, and the eigenvalues of the elasticity tensor, which reveal the mechanical stability of the structure. These quantities are shown to be correlated among each other. For example, high valence electron count is associated with low density of states,  $D$  parameter, and Pugh ratio, which in turn are indicative of low ductility. Detailed quantitative information and records of deformation type for each alloy are recorded in the Supplemental Material [26].

## II. METHODOLOGY

### A. Elastic constants

Consider a crystalline system at equilibrium, with volume  $V_0$ . If a Lagrangian strain  $\eta$  is imposed on the system, the corresponding elastic energy can be expressed as

$$\Delta E = \frac{1}{2}C_{ij}\eta_i\eta_j + O(\eta^3), \quad (1)$$

where

$$C_{ij} = \frac{1}{V_0} \left( \frac{\partial^2 E}{\partial \eta_i \partial \eta_j} \right)_{\eta=0} \quad (2)$$

is the second-order elastic constant, expressed in Voigt notation. For a cubic crystal, this has the form

$$C = \begin{pmatrix} C_{11} & C_{12} & C_{12} & 0 & 0 & 0 \\ C_{12} & C_{11} & C_{12} & 0 & 0 & 0 \\ C_{12} & C_{12} & C_{11} & 0 & 0 & 0 \\ 0 & 0 & 0 & C_{44} & 0 & 0 \\ 0 & 0 & 0 & 0 & C_{44} & 0 \\ 0 & 0 & 0 & 0 & 0 & C_{44} \end{pmatrix}. \quad (3)$$

There are only three independent elastic constants:  $C_{11}$ ,  $C_{12}$ , and  $C_{44}$ . The bulk modulus

$$K = \frac{1}{3}(C_{11} + 2C_{12}) \quad (4)$$

and the shear moduli

$$G = C_{44} \text{ or } \mu = \frac{1}{2}(C_{11} - C_{12}), \quad (5)$$

depending on the type of shear. Using the bulk and shear moduli, the Pugh ratio  $K/G$  [18] can be calculated. This ratio is a well-known measure of ductility—a high Pugh ratio is an indicator of a ductile system.

### B. Elastic stability

A system at equilibrium is elastically stable when the energy increases on application of infinitesimal strain, i.e., the elastic energy is positive. Using Eq. (1), we can express the stability criteria as

$$C_{ij}\eta_i\eta_j > 0 \text{ or } \eta^T C \eta > 0, \quad (6)$$

where  $\eta$  is any infinitesimal strain applied to the system. This condition is satisfied when  $C$  is a positive definite matrix or, equivalently, if all the eigenvalues of the second-order elastic constant matrix are positive. This is the Born stability criterion [30].

If the crystal is driven out of equilibrium by a finite strain  $\beta$ , the stability is determined by the new condition [31,32]

$$\lambda_{ij}(\beta)\eta_i\eta_j > 0 \text{ or } \eta^T \lambda(\beta)\eta > 0, \quad (7)$$

where  $\lambda(\beta)$  is the symmetrized Wallace tensor at finite strain  $\beta$  [31,32],

$$\lambda_{klmn}(\beta) = C'_{klmn}(\beta) + \frac{1}{2}[\tau_{ml}\delta_{kn} + \tau_{km}\delta_{ln} + \tau_{nl}\delta_{km} + \tau_{kn}\delta_{lm} - \tau_{kl}\delta_{mn} - \tau_{mn}\delta_{kl}], \quad (8)$$

where  $C'_{klmn}(\beta)$  is the second-order elastic constant and  $\tau$  is the Lagrangian stress tensor for the nonequilibrium crystal. For a cubic system that has been strained along the [001] axis, the symmetric Wallace tensor in Voigt notation is

$$\lambda(\beta) = \begin{pmatrix} C'_{11} & C'_{12} & C'_{13} - \frac{\tau}{2} & 0 & 0 & 0 \\ C'_{12} & C'_{11} & C'_{13} - \frac{\tau}{2} & 0 & 0 & 0 \\ C'_{13} - \frac{\tau}{2} & C'_{13} - \frac{\tau}{2} & C'_{33} + \tau & 0 & 0 & 0 \\ 0 & 0 & 0 & C'_{44} + \frac{\tau}{2} & 0 & 0 \\ 0 & 0 & 0 & 0 & C'_{44} + \frac{\tau}{2} & 0 \\ 0 & 0 & 0 & 0 & 0 & C'_{66} \end{pmatrix}. \quad (9)$$

This matrix has six eigenvectors and five unique eigenvalues. The system is stable if all the eigenvalues are positive. If one (or more) of the eigenvalues vanishes, then  $\beta$  is a critical strain for mechanical failure. The type of failure can be determined based on the eigenvector:

(i) If the critical eigenvalue has a nonzero component along the strain direction (in this case, the component  $v_3$  for an eigenvector  $v$ ), it is considered a “cleavage” [25] or “extensional” [33] instability and potentially signals a fracture of the solid [25].

(ii) If the critical eigenvalue has no component along the strain direction, it is considered a “shear” [25,33] instability. The shear mode, for some systems, can lend ductility [33,34].

### C. $\chi$ parameter

The Wallace tensor at finite strain can be approximated using the second- and third-order elastic constants at zero strain. This weakly nonlinear approach allows fast approximate calculation of the eigenvalues at different values of

finite strain. Using this approach, we can determine the critical strain  $\eta_c$ , corresponding to the first “cleavage” instability, and  $\eta_s$ , corresponding to the first “shear” instability. The intrinsic ductility parameter [24,25]

$$\chi = \frac{\eta_c}{\eta_s} \quad (10)$$

determines the system’s ability to deform via shear instability before fracture. A system is deemed ductile if the shear instability occurs before cleavage ( $\chi > 1$ ), implying that the system deforms plastically before fracture. Conversely, if the cleavage instability occurs before shear ( $\chi < 1$ ), the system is deemed brittle.

#### D. D parameter

The D parameter proposed by Rice [20,21] is another measure of ductility, given by

$$D = \frac{\gamma_s}{\gamma_{\text{usf}}}, \quad (11)$$

where  $\gamma_{\text{usf}}$  is the unstable stacking fault energy and  $\gamma_s$  is the surface energy. In this approach, ductility is thought to arise from the formation of dislocations at a crack tip, blunting the tip and hence reducing the stress. A high D-parameter corresponds to a ductile material, while a lower D-parameter corresponds to a brittle material. The D-parameter is a reciprocal of the Rice parameter [20]  $\gamma_{\text{usf}}/\gamma_s$  and is based on the Rice-Thomson parameter [19]  $Gb/\gamma_s$ , where  $G$  is the shear modulus and  $b$  is the Burgers vector. Both  $\gamma_{\text{usf}}$  and  $\gamma_s$  can be calculated directly from first principles or obtained from a surrogate model trained on first-principles data [35].

#### E. Ab initio tensile test

In this fully nonlinear approach, the second-order elastic constants and stress at finite strain are directly calculated without any extrapolations from zero strain. This is done by stretching the equilibrium structure and performing first-principles relaxation in order to obtain the structure at finite strain and the induced stress. The relaxed structure is then used to calculate the second-order elastic constants at finite strain. This is referred to as the *ab initio* tensile test. While it is computationally more intensive as compared to the weakly nonlinear  $\chi$ -parameter approach, it provides higher accuracy and significantly more insight into the behavior of the system. The first-principles relaxation allows the system to develop stacking faults, dislocations, and other interesting effects. In the following section, we discuss the application of this method in detail.

### III. TENSILE TEST OBSERVATIONS

We calculated eigenvalues, stress, and lattice distortion at fixed uniaxial strain along the [001] direction, for  $\text{Mo}_3X$  and  $\text{Nb}_3X$ , where  $X \in \{\text{Al, Cr, Hf, Nb/Mo, Re, Ru, Si, Ta, Ti, V, W, Zr}\}$ , and a set of refractory alloy-based quaternaries. 128-atom special quasirandom structures (SQS) were used. A maximum strain of 20% was applied. To gauge the size effect, tensile test was also performed for a 54-atom SQS of  $\text{Mo}_3\text{Nb}$ .

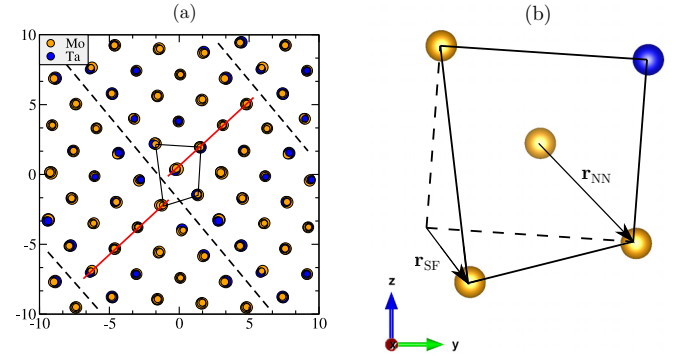


FIG. 1. (a) [100] view of  $\text{Mo}_3\text{Ta}$  at 15% uniaxial strain. Tick length units are Å. The size of the atom denotes the height of the atom in the (100) direction, with smaller atoms placed higher. Stacking faults (highlighted using red lines) occur along the [011] plane, denoted by black dashed lines. (b) A small cluster of atoms at the origin [represented by solid lines in (a)] illustrates the displacement vector  $r_{\text{SF}}$  associated with the dislocation. For this system,  $|r_{\text{SF}}| = 0.355|r_{\text{NN}}|$ , where  $|r_{\text{NN}}|$  is the nearest-neighbor separation.

No significant differences were found. Full results for the complete set of structures are provided in the Supplemental Material, along with the computational details [26]. At certain strains, the relaxed structures show interesting defects, which are discussed in the following sections.

#### A. Stacking faults

Stacking faults were observed in several alloys (see Fig. 1 and the Supplemental Material [26]). The transformation impacts the Wallace tensor eigenvalues [see Fig. 2(a)]. Examine the eigenvalues for  $\text{Mo}_3\text{Ta}$ , shown in Fig. 2(a). Eigenvectors S1, S2, and S3 represent shear modes, while C1 represents the cleavage/extensional mode. An additional extensional mode (C2) is also present; however, it is not shown in Fig. 2(a) since it is an order of magnitude larger than the others and does not affect stability. Extensional failure occurs at 13%. With further increase in strain, the system finds an alternate solution with shear failure instead of extensional—this is the stacking fault. It is unclear how this can be interpreted in terms of ductility. Shear failure is known to be an indicator of intrinsic ductility, but, in this case, it is occurring *after* extensional failure, which has been previously interpreted as fracture. The effect of the stacking fault can also be seen in the stress-strain and lattice distortion curves for  $\text{Mo}_3\text{Ta}$ , shown in Fig. 2(b). The stacking fault relieves some of the stress present in the system. It also causes a sharp increase in the lattice distortion, which is expected since the system has transformed.

#### B. Slip

Compare the  $\text{Nb}_3\text{Hf}$  structures at 12.5% and 15% strain, shown in Figs. 3(a) and 3(b). There is a noticeable rotation in the structure at 15% strain. We can understand this transformation by closely examining the structure. Figure 4 shows one particular Nb atom (located near the origin) and its near neighbors along the (100) direction. Going from 0% to 15%,

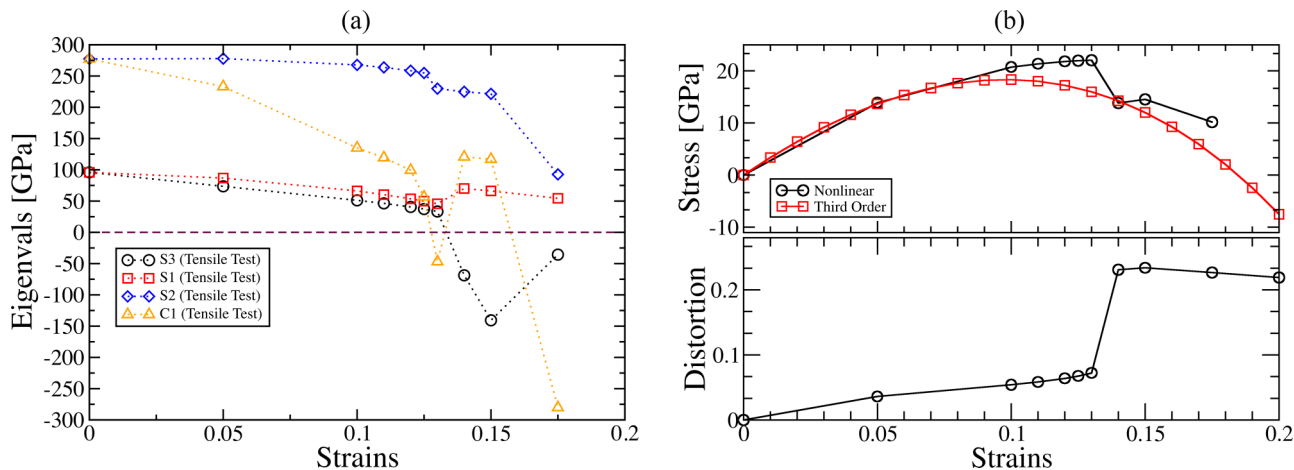


FIG. 2. (a) Wallace tensor eigenvalues of  $\text{Mo}_3\text{Ta}$  at different uniaxial strains. (b) The stress and lattice distortion (in units of  $\text{\AA}/\text{atom}$ ) of  $\text{Mo}_3\text{Ta}$  obtained from DFT at different uniaxial strain values.

we see that the species distribution of the near neighbors changes. By superimposing the clusters, we see that some of the atoms have slipped along the  $[011]$  plane. The bottom-left Nb atom, which was initially a “vertex” atom, ends up as a “body-center” atom. The body-center Hf atom on the left slips and becomes a vertex atom. This slip transformation gives rise to the rotation observed in Fig. 3(a).

This effect is observed throughout the system. Figure 5 shows a zoomed out view at 0% and 15% strain. Here we can draw the lattice planes along the same atoms in both cases. This allows us to easily view the slip plane. The Burgers vector  $b$  is along the  $[011]$  direction and  $(0\bar{1}1)$  is the glide plane which contains both the Burgers vector and the dislocation line. Since our calculations only provide the structure after the dislocation has fully passed, we cannot determine the line of dislocation.

The effect of this transformation on elastic stability can be observed from the evolution of the Wallace tensor eigenvalues. After C1 goes negative at 12.5%, there is a large

upward spike in both the C1 and S3 eigenvalues at 15% strain, restoring mechanical stability. This transformation results in a large drop in stress, as seen in Fig. 6(b). However, it is not clear if this effect helps provides ductility since it occurs after extensional failure.

### C. Twinning

Twinning is clearly seen for the  $\text{Mo}_3\text{Nb}$  system along the  $(001)$  direction [Figs. 7(a) and 7(b)]. The square bcc cells, denoted by solid black lines, become rhombus shaped. This phenomenon is referred to as the splay transformation, and transforms tetragonal structure to orthorhombic. It has been observed in previous computational studies of bcc refractory metals [33,34]. This is a shear effect and occurs in the plane perpendicular to the stretching direction. In pure Nb, the splay transformation ensures mechanical stability of the crystal and is a mechanism for intrinsic ductility.

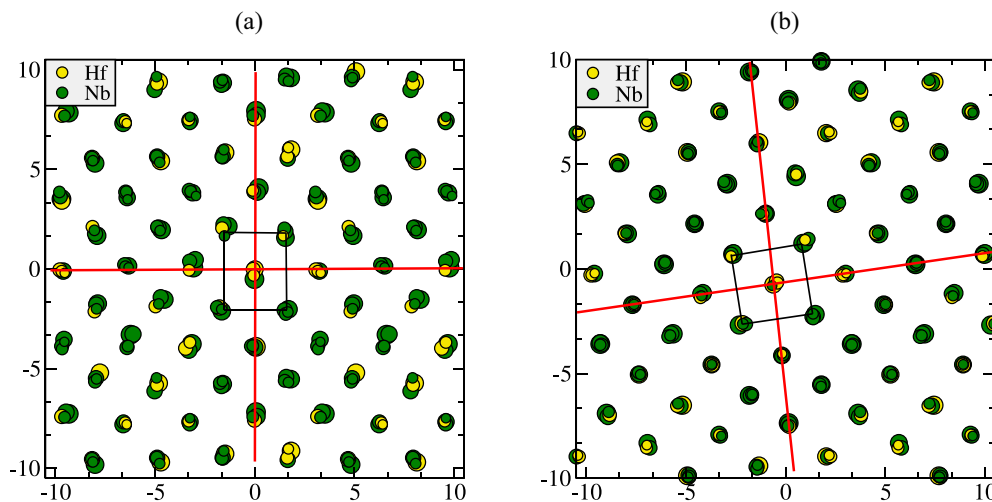


FIG. 3.  $\text{Nb}_3\text{Hf}$  at (a) 12.5% uniaxial strain and (b) 15% uniaxial strain as seen along the  $[100]$  direction. Tick length units are in  $\text{\AA}$ . The solid red lines highlight the rotation. Solid black lines represent a small cluster of atoms near the origin.

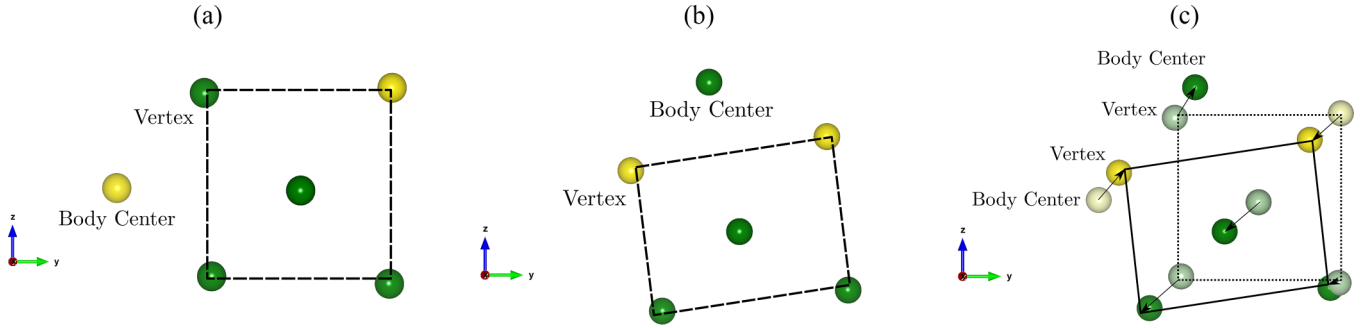


FIG. 4. Cluster of atoms taken from Fig. 3, consisting of a central atom near the origin surrounded by near neighbors, for Nb<sub>3</sub>Hf at (a) 0% and (b) 15% uniaxial strain. Both the clusters are superimposed in (c) to demonstrate the transformation. Green atoms represent Nb and gold atoms represent Hf. In (c), lighter atoms are from (a) and darker atoms are from (b).

Figure 8 shows the eigenvalues for Mo<sub>3</sub>Nb. Twinning is first observed at 17.5% strain, which is well beyond the critical strain for extensional failure. This implies that twinning does not help preserve the mechanical stability of this system and most likely does not play a role in the ductility of the alloy. For all the alloys studied in this work, the onset of twinning occurs after extensional failure. Further data on eigenvalues and twinning critical strains for all the systems that show this effect are presented in the Supplemental Material [26].

**D. No transformation**

Table I lists the alloys which show steadily increasing lattice distortion without stacking faults, slip, or twinning. The maximum stress observed for most of these systems is low in comparison to the other alloys. The Supplemental Material contains stress, lattice distortion, and eigenvalue plots for these systems [26].

**IV. ANALYSIS**

**A. Comparing existing parameters**

The Pugh ratio  $K/G$  (as defined by Pugh [18]), D parameter,  $\chi$  parameter, and the density of states at the Fermi level have all been previously used as measures of intrinsic ductility

[23,25,35–38]. It is therefore useful to check the consistency of these parameters. Figures 9(a)–9(f) show the correlations among the six possible pairs of four parameters calculated for all the binaries and quaternary systems. In most of these cases, a proportionality can be observed. A high D parameter corresponds to a high Pugh ratio, high density of states at the Fermi level, and high  $\chi$  parameter. This is consistent, as for each of these parameters a high value implies ductility and a low value implies brittle failure. The scatter in the plots reflects

TABLE I. List of the alloys which did not show any stacking faults, twinning, or slip.

	Strain at stress maximum	Stress maximum (GPa)
HfNbTiZr	0.125	2.25
Nb <sub>3</sub> Si	0.125	3.16
NbMoTiSi	0.11	3.54
Nb <sub>3</sub> Al	0.10	4.08
NbMoTiAl	0.14	4.28
Mo <sub>3</sub> Si	0.05	5.47
Mo <sub>3</sub> Ru	0.10	6.36
Mo <sub>3</sub> Al	0.11	9.59

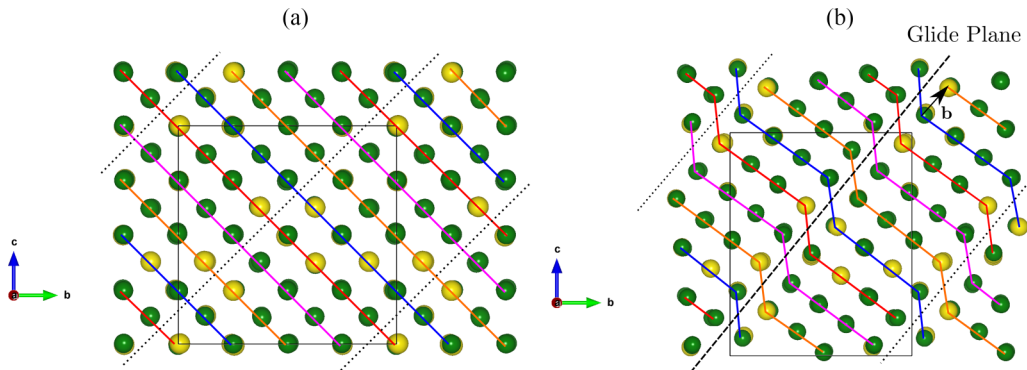


FIG. 5. Structure of Nb<sub>3</sub>Hf at (a) 0% uniaxial strain and (b) 15% uniaxial strain. The black arrow represents the Burgers vector **b**. The lattice planes are highlighted using colored lines. The glide plane, which contains both the Burgers vector and the dislocation line, is denoted by dashed lines.

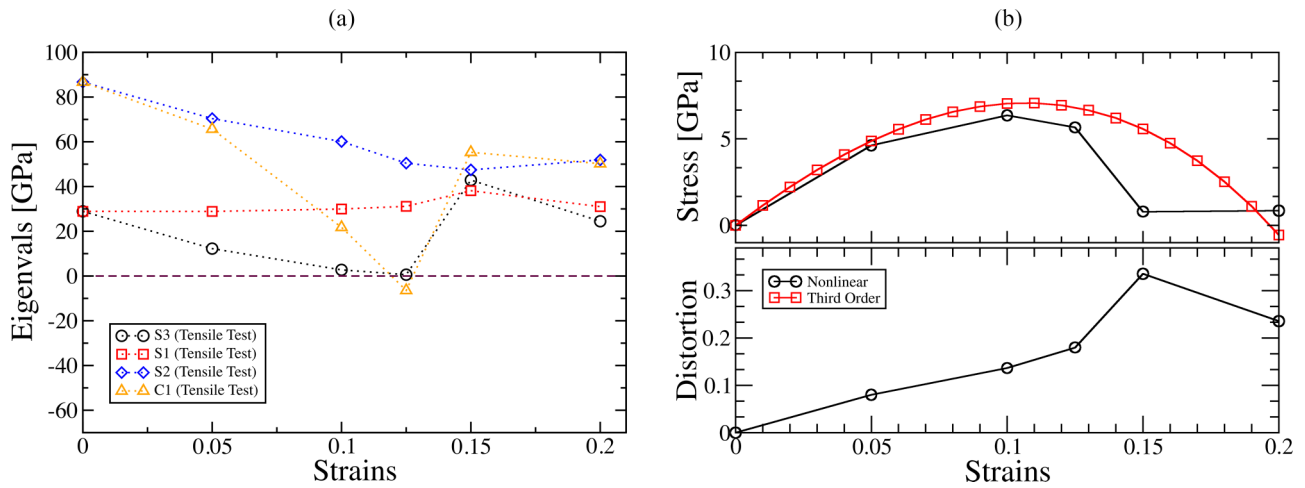


FIG. 6. (a) Wallace tensor eigenvalues of Nb<sub>3</sub>Hf at different uniaxial strains. (b) The stress and lattice distortion (in units of Å/atom) of Nb<sub>3</sub>Hf at different uniaxial strain values.

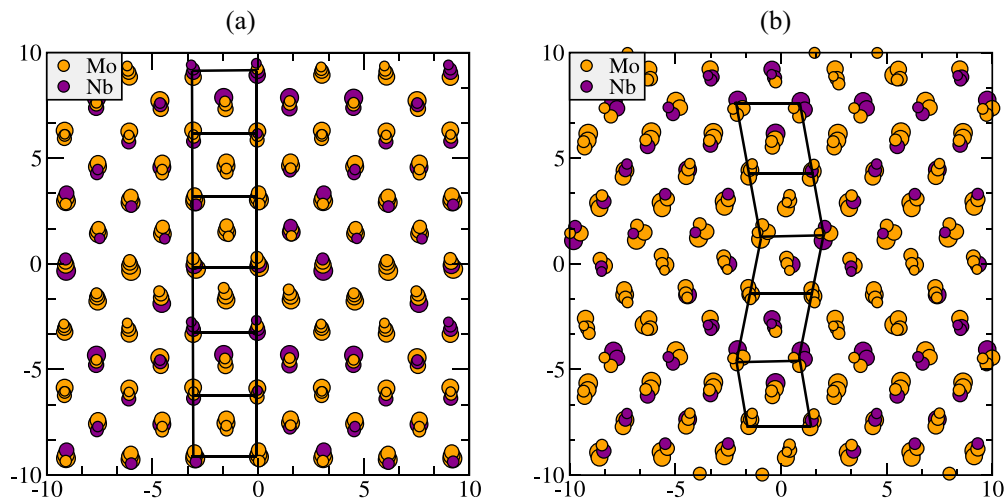


FIG. 7. Mo<sub>3</sub>Nb at (a) 15% uniaxial strain as seen along the [001] direction. The black lines denote the conventional bcc cell. (b) 20% uniaxial strain as seen along the [001] direction. The black lines denote the transformed bcc cell, resulting in twinning patterns.

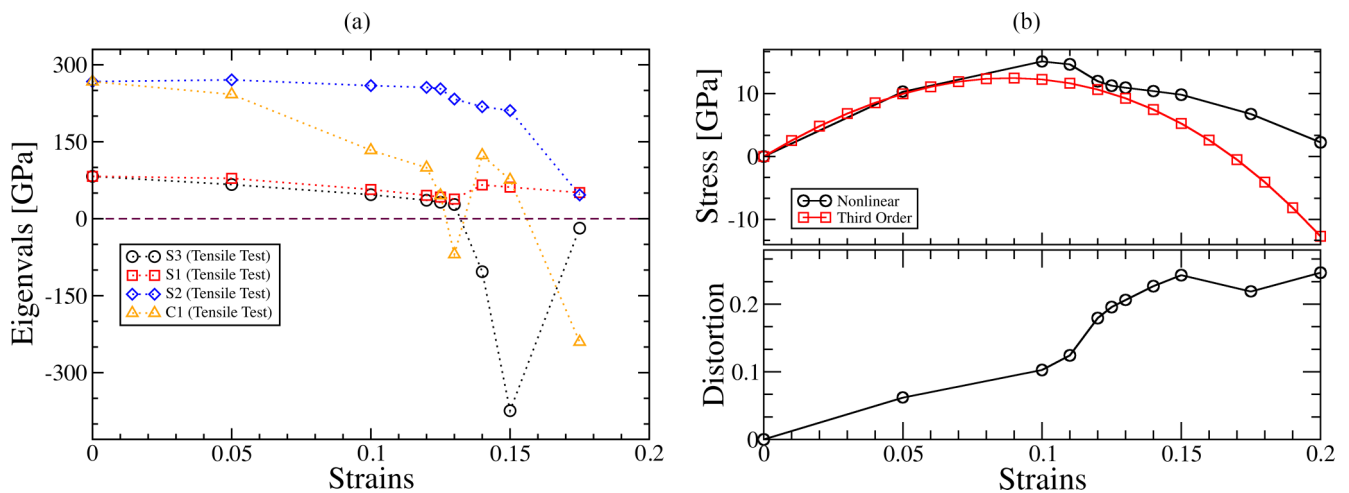


FIG. 8. (a) Wallace tensor eigenvalues for Mo<sub>3</sub>Nb. Extensional failure occurs before the structure twins. (b) The stress and lattice distortion (in units of Å/atom) of Nb<sub>3</sub>Hf at different uniaxial strain values.

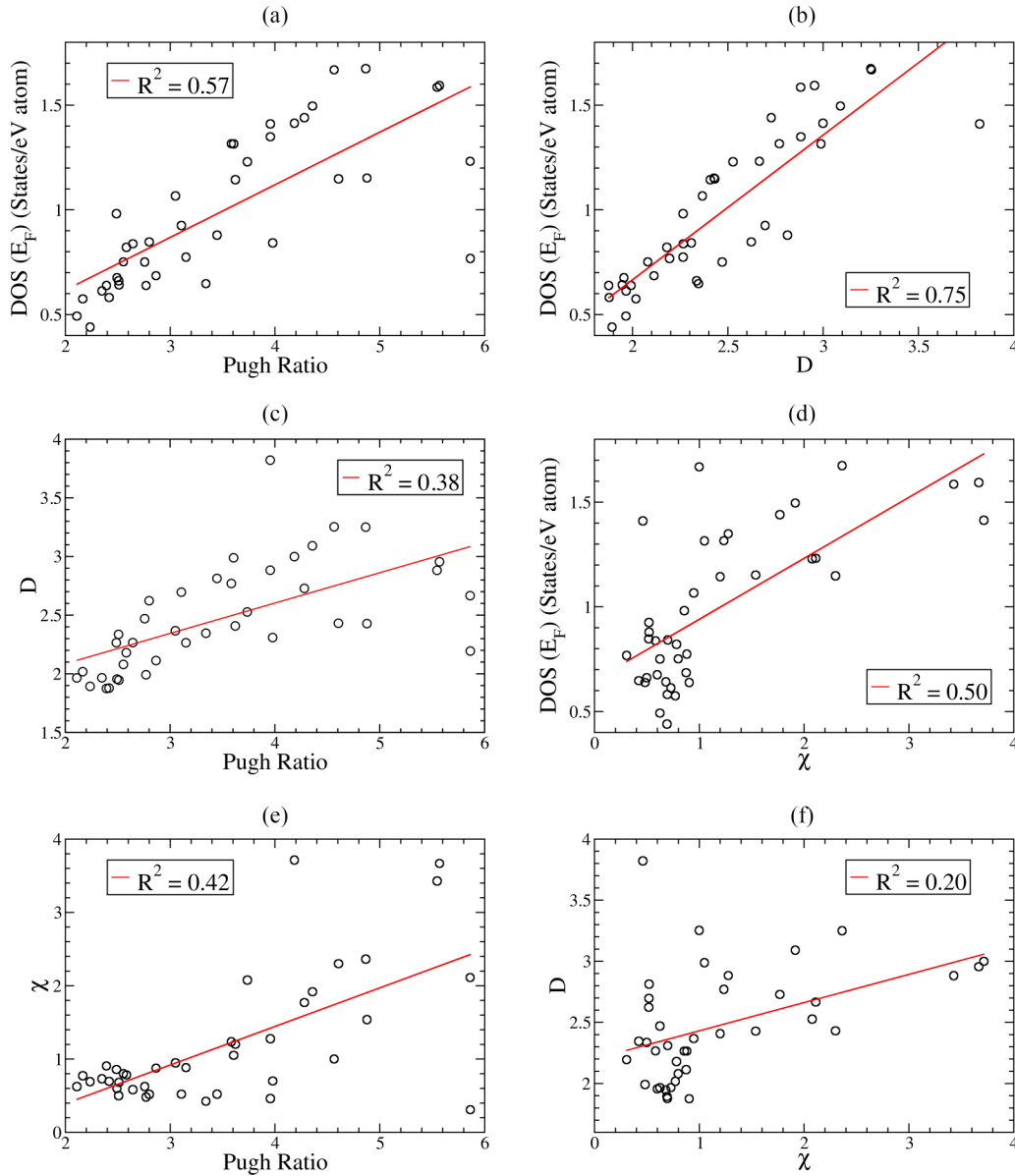


FIG. 9. Scatter plots with regression lines, comparing the existing ductility parameters D,  $\chi$ , Pugh ratio, and the density of states at the Fermi energy. The  $R^2$  values for the regression are shown in the legends of each plot.

the widely differing methodologies used for each parameter that capture different aspects of properties linked to ductility.

**B. Peak stress as a ductility parameter**

In addition to capturing stacking fault, slip, and twinning patterns, the peak stress, defined as the maximum stress obtained in the *ab initio* tensile test, functions as an intrinsic ductility parameter. To see this, we plot the tensile test peak stress against the four existing ductility parameters for all the binaries and quaternaries [Figs. 10(a)–10(d)]. With the exception of  $\chi$ , there is an inverse proportionality between the peak stress and the existing ductility parameters. This trend allows us to establish the tensile test peak stress as a ductility parameter with the inverse criteria for ductility. A high peak

stress would likely cause brittle failure, while a low peak stress would enhance ductility. The  $\chi$  parameter plot is an outlier; as with the previous case, the varying methodologies used for the parameters determine their consistency with other parameters.

**C. Valence electron count**

We compare the valence electron count (VEC) for all of the systems against the five ductility parameters, i.e., Pugh ratio, D parameter,  $\chi$  parameter, density of states at the Fermi level, and the tensile test peak stress [Figs. 11(a)–11(d) and 12]. The VEC linearly decreases with the four existing parameters and is directly proportional to the peak stress. This implies that the VEC could potentially be used as a ductility parameter—high

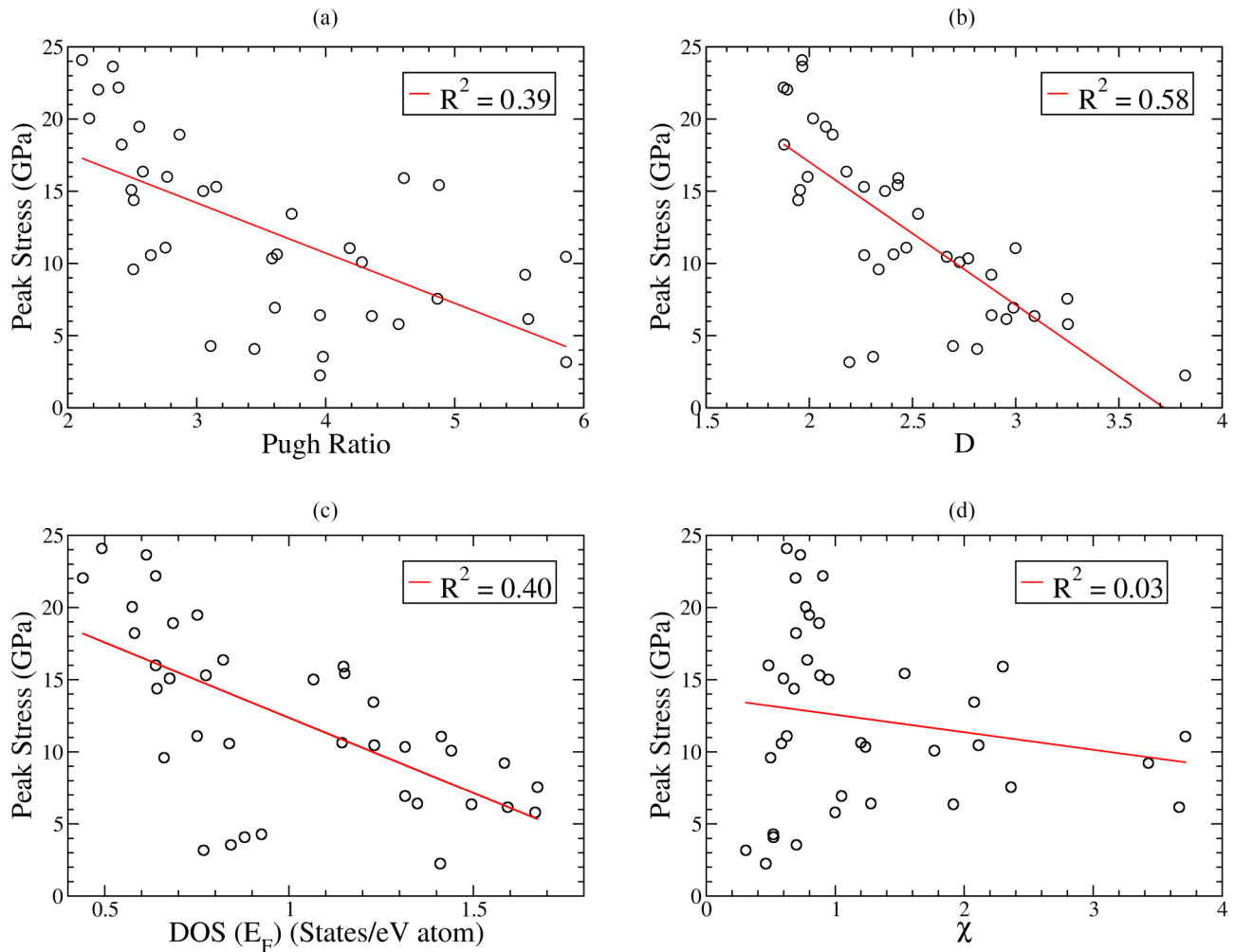


FIG. 10. Scatter plots with regression lines, comparing the peak stress obtained from *ab initio* tensile test with the existing ductility parameters  $D$ ,  $\chi$ , Pugh ratio, and the density of states at the Fermi energy. The  $R^2$  values for the regression are shown in the legends of each plot.

VEC would imply brittleness, while low VEC would imply ductility. This is a useful observation since the VEC can be obtained by simply looking at the composition and hence no calculations are required. Since many different compositions could have the same VEC, other ductility parameters will be needed for a more precise assessment. However, sorting by VEC could be a helpful preliminary step in ductile alloy design.

## V. DISCUSSION

### A. Workflow for the *ab initio* tensile test

To promote the ease of use, we provide a detailed workflow for the *ab initio* tensile test in Fig. 13. Broadly, there are two major parts to this method—careful analysis of the relaxed structures and the calculation of Wallace tensor eigenvalues at different strains. We use simple PYTHON scripts for most of the postprocessing steps, such as extracting elastic constants, stress, calculating eigenvectors, etc. All these scripts used for the postprocessing have been made available on GITHUB.[39].

Computational details for the first-principles calculations are available in the Supplemental Material [26].

### B. Comments on ductility parameters

However, there are drawbacks to using any single parameter to characterize intrinsic ductility. Every intrinsic ductility parameter has underlying assumptions that cause it to deviate from experiment. The Pugh ratio and  $\chi$  parameters assume ductility can be described by zero-strain second-order elastic constants. The  $D$  parameter assumes ductility arises from crack tip blunting, which is only one of several possible mechanisms that could provide ductility. The tensile test approach also relies on elastic constants, albeit at finite strain. Since each model parameter is idealized in different ways, precise agreement between the parameters is not expected. We can see this from the scatter plots of Figs. 9–12. There are useful general trends, which we discussed in the previous section, but there is also significant variance from the least-squares fit. These parameters are useful when applied to a large number of systems in order to identify a group of potentially

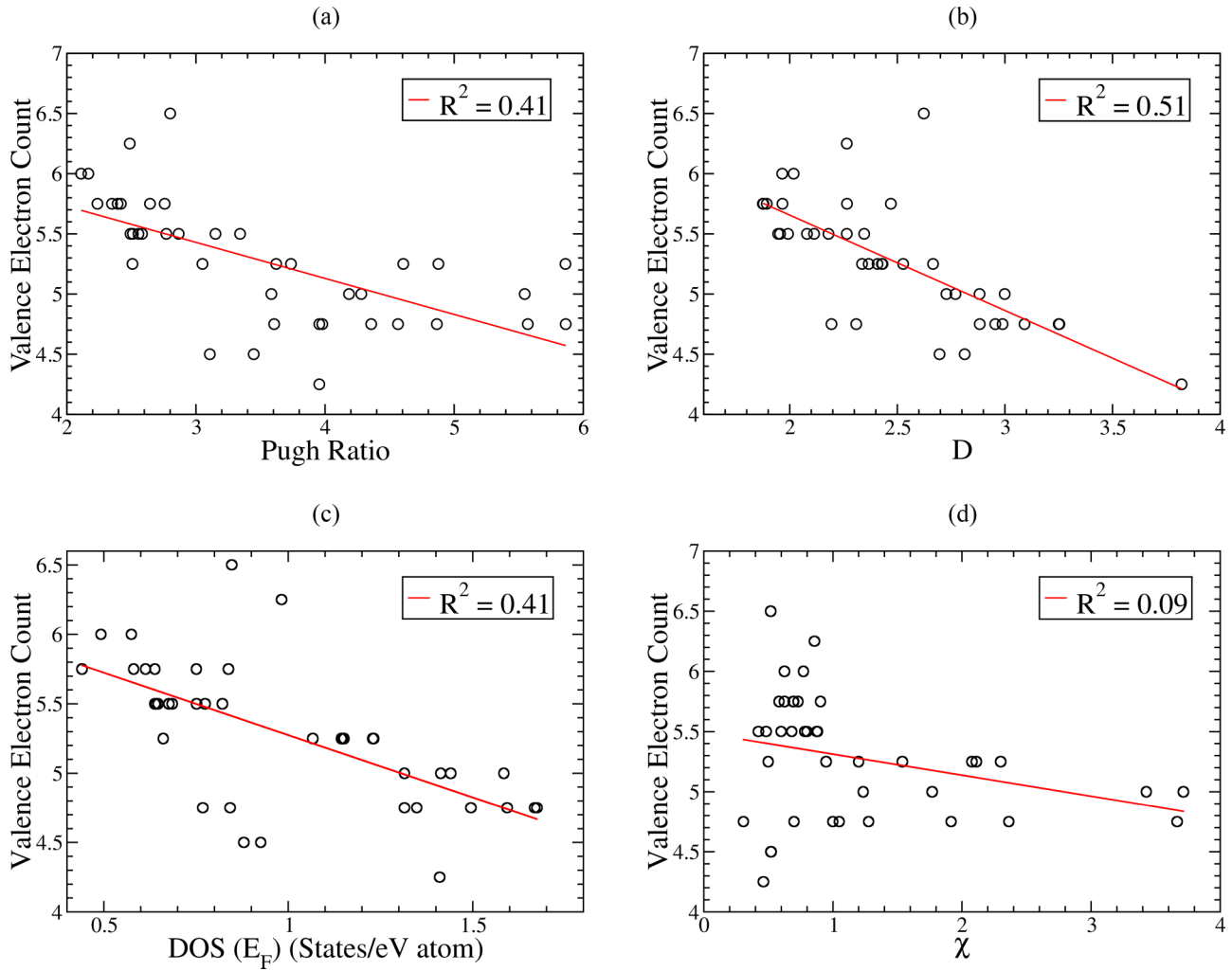


FIG. 11. Scatter plots with regression lines, comparing the VEC with the existing ductility parameters  $D$ ,  $\chi$ , Pugh ratio, and the density of states at the Fermi energy. The  $R^2$  values for the regression are shown in the legends of each plot.

ductile compositions. But when analyzing specific alloys, these parameters provide conflicting assessments of the

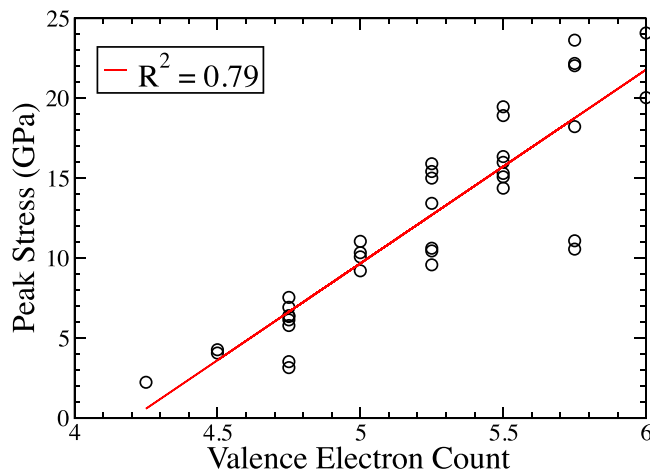


FIG. 12. Scatter plot with regression lines, comparing the VEC with the tensile test peak stress. The  $R^2$  values for the regression are shown in the legend.

ductility. Fine-grained analysis of ductility requires realistic simulations, which include defects and grain boundaries and account for all the possible ductility providing mechanisms that could arise in the system. The *ab initio* tensile test is a small step in that direction, since it produces realistic effects such as slip and twinning that occur at large strains. However, we still use idealized unit cells. Performing the *ab initio* tensile test on very large unit cells with different grains would be an interesting future project which could produce more exciting results. Soft phonon modes with nonzero wave number can contribute to the elastic stability in bcc structures [40]. However, calculating the phonon spectra for the strained supercell structures is an extremely intensive task and has been left as a future exercise. Obtaining a material agnostic parameter that can accurately and reliably predict ductility is an extremely complicated proposition and still remains an open problem in the field.

## VI. CONCLUSION

In this work, we used the *ab initio* tensile test method to study intrinsic ductility. This method was applied to a

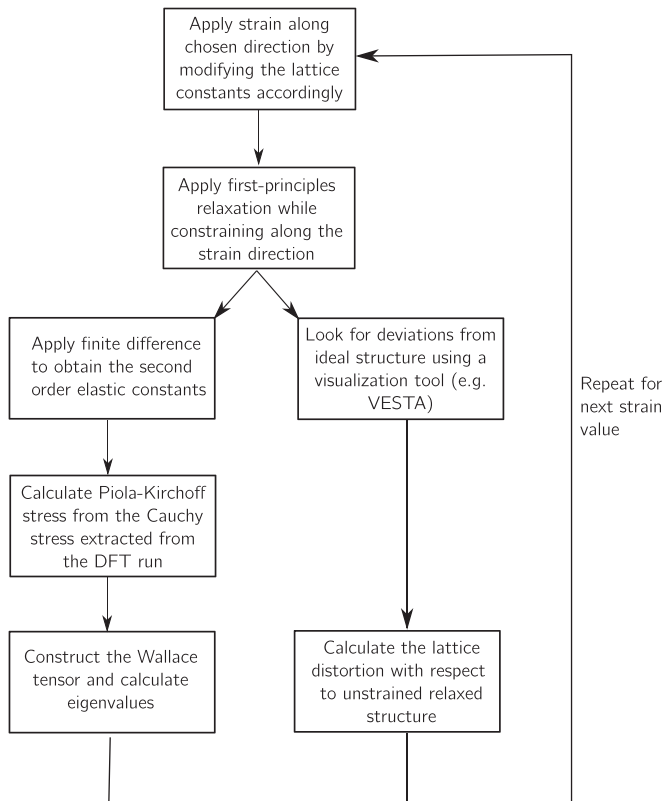


FIG. 13. Chart illustrating the workflow for the *ab initio* tensile test method.

large number of Mo- and Nb-based binaries and various failure mechanisms, such as twinning, stacking fault, and slip, were uncovered. The eigenvalues of the symmetric Wallace tensor were also calculated, and nonmonotonicities in the eigenvalue-strain curves were correlated with the different failure modes. The peak stress and VEC were linked to ductility by comparing them to the D parameter,  $\chi$  parameter, Pugh ratio, and the density of states at the Fermi level, all of which have been previously used as indicators of ductility. The differences and limitations of this method were discussed, along with the difficulties in accurate ductility estimation. Finally, we provide some ideas for improving the *ab initio* tensile test approach.

### ACKNOWLEDGMENTS

This work was supported by the ARPA-E program at CMU (Grant No. DE-AR0001430) and at NETL. This work was funded by the Department of Energy, ARPA-e, an agency of the U.S. Government. It was also supported by the Department of Energy Grant No. DE-SC0014506. We acknowledge useful discussions with Amit Samanta (LLNL) on ductility parameter analysis. This research used resources of the National Energy Research Scientific Computing Center (NERSC), a U.S. Department of Energy Office of Science User Facility supported by the Office of Science under Contract No. DE-AC02-05CH11231 using NERSC Award No. ALCC-ERCAP0022624.

- [1] P. Singh, A. Sharma, A. V. Smirnov, M. S. Diallo, P. K. Ray, G. Balasubramanian, and D. D. Johnson, Design of high-strength refractory complex solid-solution alloys, *npj Comput. Mater.* **4**, 16 (2018).
- [2] C. Lee, F. Maresca, R. Feng, Y. Chou, T. Ungar, M. Widom, K. An, J. D. Poplawsky, Y. Chou, P. K. Liaw, and W. A. Curtin, Strength can be controlled by edge dislocations in refractory high-entropy alloys, *Nat. Commun.* **12**, 5474 (2021).
- [3] O. N. Senkov, D. B. Miracle, K. J. Chaput, and J.-P. Couzinie, Development and exploration of refractory high entropy alloys—A review, *J. Mater. Res.* **33**, 3092 (2018).
- [4] X. Xie, N. Li, W. Liu, S. Huang, X. He, Q. Yu, H. Xiong, E. Wang, and X. Hou, Research progress of refractory high entropy alloys: A review, *Chin. J. Mech. Eng.* **35**, 142 (2022).
- [5] V. Sorkin, Z. G. Yu, S. Chen, T. L. Tan, Z. H. Aitken, and Y. W. Zhang, A first-principles-based high fidelity, high throughput approach for the design of high entropy alloys, *Sci. Rep.* **12**, 11894 (2022).
- [6] R. Feng, C. Zhang, Michael C. Gao, Zongrui Pei, F. Zhang, Y. Chen, D. Ma, K. An, J. D. Poplawsky, L. Ouyang, Y. Ren, J. A. Hawk, M. Widom, and P. K. Liaw, High-throughput design of high-performance lightweight high-entropy alloys, *Nat. Commun.* **12**, 4329 (2021).
- [7] X. Xing-Hong, Z. Jun, C. Xiang-Rong, and Y. Wei-Qing, Elastic constants of NaCl under pressure via first-principles calculations, *Chin. Phys. Lett.* **23**, 2845 (2006).
- [8] S. Shang, Y. Wang, and Z. Liu, First-principles elastic constants of  $\alpha$  and  $\theta$ -Al<sub>2</sub>O<sub>3</sub>, *Appl. Phys. Lett.* **90**, 101909 (2007).
- [9] M. J. Mehl, B. M. Klein, and D. A. Papaconstantopoulos, *Intermetallic Compounds: Principles*, edited by J. H. Westbrook and R. L. Fleischer (John Wiley and Sons, New Jersey, 1994) Vol. 1.
- [10] R. P. Thompson and W. J. Clegg, Predicting whether a material is ductile or brittle, *Curr. Opin. Solid State Mater. Sci.* **22**, 100 (2018).
- [11] S. Kalpakjian, *Manufacturing Processes for Engineering Materials* (Addison-Wesley, Boston, 1984).
- [12] D. Hull and D. J. Bacon, *Introduction to Dislocations*, 4th ed. (Butterworth-Heinemann, Oxford, 2001).
- [13] J. P. Hirth and J. Lothe, *Theory of Dislocations*, 2nd ed. (John Wiley and Sons, New Jersey, 1982).
- [14] T. H. Courtney, *Mechanical Behavior of Materials*, 2nd ed. (McGraw-Hill, New York, 2000).
- [15] G. Frommeyer, U. Brück, and P. Neumann, Supra-ductile and high-strength manganese-TRIP/TWIP steels for high energy absorption purposes, *ISIJ Intl.* **43**, 438 (2003).
- [16] F. D. Fischer, Q. P. Sun, and K. Tanaka, Transformation-induced plasticity (TRIP), *Appl. Mech. Rev.* **49**, 317 (1996).
- [17] F. D. Fischer, G. Reisner, E. Werner, K. Tanaka, G. Cailletaud, and T. Antretter, A new view on transformation induced plasticity (TRIP), *Intl. J. Plast.* **16**, 723 (2000).
- [18] S. F. Pugh, XCII. Relations between the elastic moduli and the plastic properties of polycrystalline pure metals, *London Edinburgh Dublin Philos. Mag. J. Sci.* **45**, 823 (1954).

- [19] J. Rice and R. Thomson, Ductile versus brittle behaviour of crystals, *Philos. Mag.* **29**, 73 (1974).
- [20] J. Rice, Dislocation nucleation from a crack tip: An analysis based on the Peierls concept, *J. Mech. Phys. Solids* **40**, 239 (1992).
- [21] M. Mehl, D. Papaconstantopoulos, N. Kioussis and M. Herbranson, Tight-binding study of stacking fault energies and the Rice criterion of ductility in the fcc metals, *Phys. Rev. B* **61**, 4894 (2000).
- [22] Z. Wu and W. Curtin, Brittle and ductile crack-tip behavior in magnesium, *Acta Mater.* **88**, 1 (2015).
- [23] P. Tu, Y. Zheng, C. Zhuang, X. Zeng, and H. Zhu, A high-throughput computation framework for generalized stacking fault energies of pure metals, *Comput. Mater. Sci.* **159**, 357 (2019).
- [24] M. de Jong, I. Winter, D. C. Chrzan, and M. Asta, Ideal strength and ductility in metals from second- and third-order elastic constants, *Phys. Rev. B* **96**, 014105 (2017).
- [25] I. S. Winter, M. de Jong, J. Montoya, E. Rothchild, and D. C. Chrzan, Intrinsic ductility of random substitutional alloys from nonlinear elasticity theory, *Phys. Rev. Mater.* **3**, 113608 (2019).
- [26] See Supplemental Material at <http://link.aps.org/supplemental/10.1103/PhysRevMaterials.7.123601> for detailed quantitative information and records of deformation type for each alloy. The Supplemental Material also contains Refs. [27–29].
- [27] G. Kresse and D. Joubert, From ultrasoft pseudopotentials to the projector augmented-wave method, *Phys. Rev. B* **59**, 1758 (1999).
- [28] J. P. Perdew, K. Burke, and M. Ernzerhof, Generalized gradient approximation made simple, *Phys. Rev. Lett.* **77**, 3865 (1996).
- [29] M. Methfessel and A. T. Paxton, High-precision sampling for Brillouin-zone integration in metals, *Phys. Rev. B* **40**, 3616 (1989).
- [30] M. Born, On the stability of crystal lattices. I, *Math. Proc. Camb. Phil. Soc.* **36**, 160 (1940).
- [31] D. C. Wallace, *Thermodynamics of Crystals* (Dover, Mineola, NY, 1998).
- [32] J. W. Morris Jr. and C. R. Krenn, The internal stability of an elastic solid, *Philos. Mag. A* **80**, 2827 (2000).
- [33] V. Raghuraman, M. Widom, and M. C. Gao, Nonlinear deformation and elasticity of BCC refractory metals and alloys, *Phys. Rev. Mater.* **6**, 053601 (2022).
- [34] L. Qi and D. C. Chrzan, Tuning ideal tensile strengths and intrinsic ductility of bcc refractory alloys, *Phys. Rev. Lett.* **112**, 115503 (2014).
- [35] Y.-J. Hu, A. Sundar, S. Ogata, and L. Qi, Screening of generalized stacking fault energies, surface energies and intrinsic ductile potency of refractory multicomponent alloys, *Acta Mater.* **210**, 116800 (2021).
- [36] Y. X. Ye, B. L. Musico, Z. Z. Lu, L. B. Xu, Z. F. Lei, V. Keppens, H. X. Xu, and T. G. Nieh, Evaluating elastic properties of a body-centered-cubic NbHfZrTi high-entropy alloy—A direct comparison between experiments and *ab initio* calculations, *Intermetallics* **109**, 167 (2019).
- [37] X. J. Gu, S. J. Poon, G. J. Shiflet, and M. Widom, Mechanical properties, glass transition temperature, and bond enthalpy trends of high metalloid Fe-based bulk metallic glasses, *Appl. Phys. Lett.* **92**, 161910 (2008).
- [38] X. J. Gu, S. J. Poon, G. J. Shiflet, and M. Widom, Ductility improvement of amorphous steels: Roles of shear modulus and electronic structure, *Acta Mater.* **56**, 88 (2008).
- [39] <https://github.com/vishnu2709/ElasticToolkit.git>
- [40] K. Persson, M. Ekman, and V. Ozoliņš, Phonon instabilities in bcc Sc, Ti, La, and Hf, *Phys. Rev. B* **61**, 11221 (2000).